This document is the unedited Author's version of a Submitted Work that was subsequently accepted for publication in 'Nano Letters', copyright © American Chemical Society after peer review. To access the final edited and published work see https://doi.org/10.1021/acs.nanolett.0c02558

Nanofluidics for Simultaneous Size and Charge Profiling of Extracellular Vesicles

Imman I Hosseini,[†] Zezhou Liu,[‡] Xavier Capaldi,[‡] Tamer Abdelfattah,[†] Laura Montermini,[¶] Janusz Rak,[¶] Walter Reisner,[*,‡] and Sara Mahshid[*,†]

†*Department of Biomedical Engineering, McGill University, 3775 rue university, Montreal, Quebec H3A 2B4, Canada*

‡*Department of Physics, McGill University, 3600 rue university, Montreal, Quebec H3A 2T8, Canada*

¶*Department of Pediatrics, McGill University, 3775 rue university, Montreal, Quebec H3A 2B4, Canada*

E-mail: reisner@physics.mcgill.ca; sara.mahshid@mcgill.ca

Phone: +1 (514) 398-3058; +1 (514) 398-8964

Abstract

Extra-cellular vesicles (EV's) are cell-derived membrane structures that circulate in body fluids and show considerable potential for non-invasive diagnosis. EVs possess surface chemistries and encapsulated molecular cargo that reflect the physiological state of cells from which they originate, including the presence of disease. In order to fully harness the diagnostic potential of EVs, there is a critical need for technologies that can profile large EV populations without sacrificing single EV level detail by averaging over multiple EVs. Here we use a nanofluidic device with tunable confinement to trap EVs in a free energy landscape that modulates vesicle dynamics in a manner dependent on EV size and charge. As proof-of-principle, we perform size and charge profiling of a population of EVs extracted from human glioblastoma astrocytoma (U373) and normal human astrocytoma (NHA) cell-lines.

Keywords

Extracellular vesicles, tunable confinement, nanofluidics

Cells continuously secrete membrane vesicles into the extracellular environment. These vesicles, known as extra-cellular vesicles (EV's), transport a broad range of molecular cargoes, including proteins and nucleic acids, enabling intra-cellular exchange of molecular components.[1,2] EV driven exchange plays an important role in maintaining normal bodily homeostasis;[3] EV cargo may also contain markers indicating the presence of disease in the originating cells,[2] such as cancer.[4] As EVs circulate in the blood, they can be sampled without need for invasive tissue biopsy,[5] offering hope for a rapid, risk-free diagnosis or real-time monitoring of a known disease.[4]

EV based diagnostics face substantial challenges due to the small size of EVs and their biochemical complexity; an additional challenge is the extreme heterogeneity of EV populations.[6] Circulating EV's derive from a wide-range of cell-types, including cells that do not exhibit any underlying pathology.[3] Circulating EVs also arise from distinct biogenesis processes.[1,2] One class of EVs, known as exosomes (50-100 nm in diameter), are formed when multi-vesicle endosomes (MVE's) fuse to the cell membrane and release their intraluminal vesicles into the extra-cellular environment. A second class of EVs, known as microvesicles (50-1000 nm in diameter), arise from outward budding and fission of the cell plasma membrane (blebbing). Both exosomes and microvesicles have diagnostic significance in cancer, with physical properties and co-expressed oncogenic mutations that reflect a single originating tumor cell. Heterogeneity is also observed within each subgroup. Exosomes may be formed via different mechanisms, including Endosomal Sorting Complex Required for Transport (ESCRT),[7] ESCRT- independent machineries[8] and tetraspanin proteins,[9] with each distinct mechanism leading to different molecular cargo. Exosomal content may also be size dependent.[10] Microvesicles are also formed via different blebbing mechanisms, e.g. increases in cytosolic Ca_2^+ levels on plasma membrane,[11] or activation of P2X receptors.[12]

Tumorgenesis and consequent treatment regimes may also influence EV heterogeneity. Cancer's incredible molecular complexity arises through selection pressures operating in the spatially complex and dynamic tumor microenvironment.[13–15] When a tumor cell acquires a specific driver mutation conferring a fitness advantage, the cell will proliferate rapidly giving rise to a clonal population containing the initial driver. These clonal populations will then undergo successive sub-differentiation as cells interact with/reorganize their surroundings, undergo metastasis to colonize far-flung regions of the body and acquire mutations to overcome drug therapy. Sampled EV populations may contain molecular signatures of this underlying dynamics,[13,16] which in turn may have crucial implications for treatment (e.g. providing early warning of the emergence of resistant tumor cell sub-populations[15]).

Standard molecular analyses of bulk EVs by polymerase chain reaction (PCR) and other methods require 'averaging' of diagnostic signals. Averaging implies that the diagnostically crucial single-cell level information carried by each EV is lost against high backgrounds of irrelevant and/or normal cells. For example, classical bench-top EV analysis protocols typically use μL to mL of sample (containing $10^5 - 10^8$ of exosomes[17]). Microfluidic approaches for EV isolation/analysis reduce sample size requirements.[18] Yet these platforms, which typically use immunoaffinity to capture EVs with pre-selected markers, still average over many EVs, in particular requiring the binding of multiple EV's to microbeads[19] or device surfaces[20] (the best platforms average over > 10 EV's[19]).

In order to fully harness the potential of EV based diagnostics, there is need to develop platforms that can output multiple interrelated disease markers from a single EV. The ability to output multiple disease markers on a single EV basis can not only increase the level of biomedically relevant detail, for example for improved prognosis and prediction, but also increase the number of diagnostically significant marker combinations available, thereby increasing the chances of disease detection. Here we harness a nanofluidic system incorporating tunable confinement to output the size and charge of individual EVs analyzed in parallel over an array of nanofluidic traps. EV charge arises from surface associated molecules (e.g. proteins,[1] glycans[21] and cholesterol[22]) that are incorporated during biogenesis. EV charge is one of the predominant factors to uptake by the receiving cell.[23]

Moreover, EVs from prostate cancer cells have a higher charge (PC3) than normal prostate epithelial cells (PNT2) possibly due to their higher concentration of sialic acids,[24] and therefore EV charge is a potential cancer biomarker.

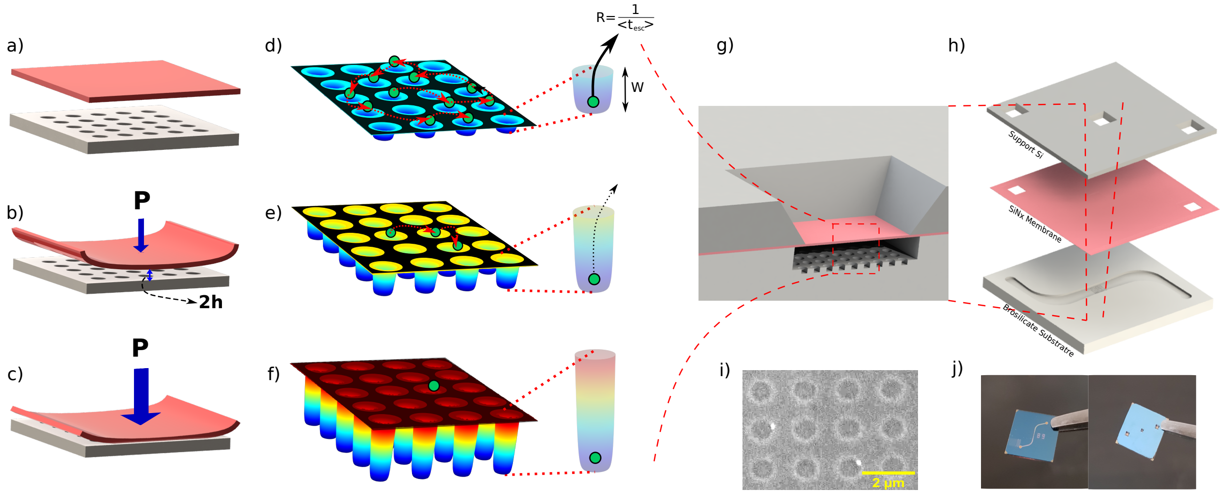

Figure 1: (a) The device consists of a lattice of circular nanocavities bonded to a flexible membrane lid. (b) When pneumatic pressure P is applied to the lid, the lid is deflected downwards, increasing the degree of vertical confinement experienced by the particles. At maximum deflection (c), the confinement is complete and the particles cannot escape from the cavities. (d-f) The imposed confinement alters the electrostatic free energy landscape experienced by the particle, increasing the potential well depth W for a particle confined in a cavity, which in turn decreases the particle escape rate R. (g-h) The device consists of a nanoslit with embedded cavity lattice etched into a borosillicate substrate. A flexible nanoscale nitride lid is exposed at the device center and suspended over the cavity lattice. The nanoslit is interfaced to two loading ports for introducing particle containing solution. (i) SEM of cavities taken through the nanoscale lid. (j) photograph of $1 \times 1\,\mathrm{cm}$ device.

Our device consists of an array of nanocavities embedded in a nanoslit (Fig. 1(a)). A flexible nanoscale lid is deflected downwards by pneumatic pressure (Fig. 1(b)),[25,26] varying the degree of vertical confinement experienced by vesicles in the nanoslit. At the highest membrane deflection, the cavities are closed-off from the surrounding slit, isolating single vesicles in the cavities (Fig. 1(c)). This and closely related approaches[27–37] have been applied to a range of trapping/physical confinement applications, including trapping of single nanoparticle's,[28,29,32,33] ds/ss DNA[25,26,30,31] and chromatin.[34] Here we exploit the capability of such devices to directly vary the escape rate (R_{esc}) of vesicles from the well by varying the surrounding confinement. The escape rate, equivalent to the inverse average time of escape of a vesicle from a cavity ($\langle t_{\mathrm{esc}} \rangle$), is determined by the depth of the free energy well experienced by a confined vesicle (Fig. 1(d-f)).[38–40] In low ionic strength buffer, this potential well depth (DPW, or Depth of Potential Well, W), has a strong dependence on electrostatics, so that measurement of the escape rate can access both the size and charge of single vesicles, an approach termed single-molecule electrometry.[39,41] By combining the single-molecule electrometry with tunable confinement, we gain the ability to make precision measurements of charge on a single-vesicle basis, due to the ability to perform multiple measurements of escape rate of a single vesicle for different degrees of confinement. Critically, our flexible lid constructed from a nanoscale silicon nitride membrane is sufficiently rigid so that the DPW is constant over a number of cavities (Fig. 1(d-f)), enabling acquisition of sufficient statics on particle trajectories to make precise measurements of escape-rate. As our approach can also access Brownian diffusion of vesicles in the slit between cavities, we can also measure vesicle size, comparable to Nanoparticle Tracking Analysis (NTA). Note that NTA yields only particle size, while our approach yields both size and charge for each vesicle. As proof-of-principle, we probe both the size and charge of EVs extracted from a human glioblastoma astrocytoma cell-line (U373) and benchmark these results against equivalent measurements taken from the healthy counterpart cell line (normal human astrocytoma, NHA).

Our tunable confinement device is fabricated using the approach outlined in Capaldi *et al.*[25] In detail, the device consists of a borosillicate substrate containing a lattice of circular nanocavities (radius $R_{\mathrm{c}} = 500\,\mathrm{nm}$), embedded 200 nm deep in a 400-500 nm deep nanoslit connected to two loading reservoirs (Fig. 1(g, h), see Sup. Mat. I). A free-standing 100 nm

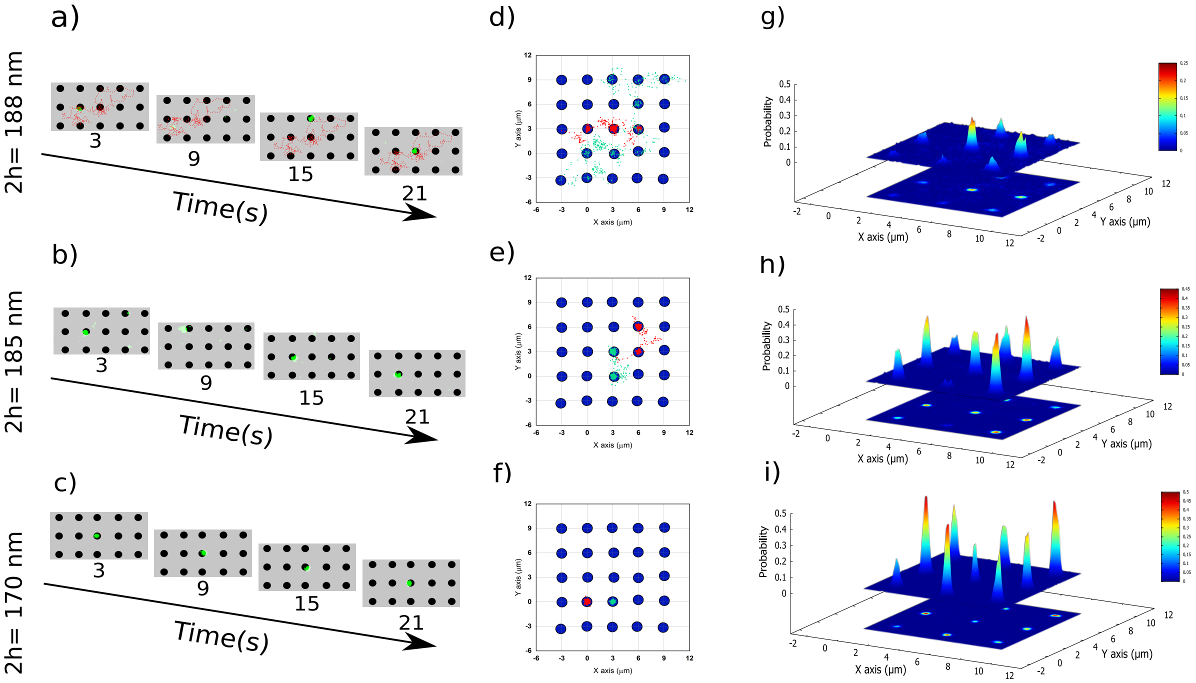

Figure 2: (a-c) Sequence of fluorescence micrographs of plasmids diffusing in cavity lattice for (a) weak, (b) moderate and (c) strong confinement. The cavity positions are indicated in gray. (d-f) Corresponding trajectories for three example plasmids for (d) weak, (e) moderate and (f) strong confinement. (g-i) The probability of finding the plasmid at a point in the cavity lattice, for (g) weak, (h) moderate and (i) strong confinement. At higher confinement the plasmids remain in the cavities longer relative to the slit, resulting in a higher probability for a plasmid to be found in a cavity.

thick silicon nitride membrane is exposed in the device center, forming a flexible lid over the nanoslit. The device is secured to a 3D printed chuck via a membrane gasket. The chuck contains access ports for injecting particle containing buffer solution as well as application of pneumatic pressure to depress the membrane. Prior to operating the device, the nanoslit is incubated in PVP solution to prevent vesicle adhesion. The chuck is mounted in a fluorescence microscopy setup with LED-based multi-wavelength illumination. When the membrane is deflected by applied pneumatic pressure, the vertical gap (slit height) is decreased. We calibrate the slit height as a function of pressure by measuring the intensity of fluorescent dye in the nanoslit (see Sup. Mat. II). Note that the gap height varies across the membrane (see Fig. 1(b,c)); we perform measurements only over the portion of the membrane with a gap height varying less than a fixed threshold $2\delta h_{\mathrm{max}}$, which we call the plateau region (see inset to Fig. S8 in Sup. Mat. XII for definition of plateau region). Experiments were primarily performed in devices with $\delta h_{\mathrm{max}} = 0.8\,\mathrm{nm}$, with a corresponding 'plateau region no smaller than the 6×5 array of cavities in the device center (the total membrane area was $160{\times}200\,\mu\mathrm{m}^2$ and the slit was 500 nm deep). A second device class used a larger $\delta h_{\mathrm{max}} = 10\,\mathrm{nm}$ (plateau region corresponded to 6×6 array of cavities in the device center, total membrane area was $100{\times}100\,\mu\mathrm{m}^2$ and slit depth was 400 nm). Height measurements are determined as an average over the gap heights in the plateau region.

We choose low ionic strength buffer conditions to ensure that the confining free energy well at each lattice site is determined by electrostatics (we use 1mM Tris with 0.4 mM NaCl solution, yielding an ionic strength $I = 0.7\,\mathrm{mM}$ and a Debye length of 11.5 nm, see Sup. Mat. III). A charged particle confined between two parallel like-charged confining surfaces has an equilibrium position, or potential energy minima, lying at the mid-point between the two surfaces.[41,42] At the position of an embedded cavity, this mid-point potential energy minima will lie inside the cavity and be lower than the mid-point potential minima in the surrounding slit. Consequently, an energy barrier will exist preventing particle escape from the well, given by the potential difference between the inside and outside of the cavity;

this is the potential well depth (DPW, W). The DPW can be computed by solving the Poisson-Boltzmann equation for the circular cavity geometry,[43] and depends in detail on the buffer ionic strength, zeta potential of confining surfaces (ψ_s), and the device geometry, including the cavity radius (R_c), cavity depth (d), and the slit height ($2h$). By varying the slit height via our tunable confinement capability, we directly modulate the DPW, and therefore modulate the particle residency time in the cavity traps (see Fig. 1(d-f) for examples of the electrostatic potential landscape for different gap heights computed from the PB equation).

We use fluorescently labeled plasmids (pBR322g, New England Biosciences) to benchmark and calibrate the tunable confinement device for single vesicle electrometry. The plasmids, all possessing the same sequence, have a uniform chemistry, so differences in behavior between individual plasmids arise necessarily from Brownian dynamics and not intrinsic chemical heterogeneity. We find that, as expected, plasmid diffusive dynamics in the cavity lattice depends strongly on the degree of imposed confinement (Fig. 2, also see supplementary movie). When confinement is weak, particles transit rapidly between many cavities over the minute long movie (Fig. 2(a, d)) with a low residency time in each cavity (Fig. 2(g)). In this case the DPW is low and it is highly probable that a thermal fluctuation will drive the plasmid out of a well at any given instant. Once a plasmid escapes from the well, the plasmid diffuses in the nanoslit until it reaches the next local energy minimum. At an intermediate degree of confinement, the DPW is higher and particles can explore only a limited number of wells over the course of the movie (Fig. 2(b, e)), with a higher residency time in each well (Fig. 2(h)). Finally, at the highest confinement, the plasmids are trapped in a single well over the entire movie (Fig. 2(c, f, i)).

By quantifying the plasmid trajectories in the cavity lattice we can deduce the distribution of plasmid escape times from the well t_{esc} for each confinement condition (Sup Mat. IV). The escape times follow an exponential distribution (Fig. 3(a-c)), as expected for a Poisson process. The average escape time $\langle t_{\text{esc}} \rangle$ is obtained from fitting an exponential model to the escape time distributions: $P(\Delta t) = A/\langle t_{\text{esc}} \rangle \exp(-\Delta t/\langle t_{\text{esc}} \rangle)$. The quantity $\langle t_{\text{esc}} \rangle$ increases strongly with increasing confinement (decreasing slit height $2h$, Fig. 3(d)). Note that Fig. 3(d) includes measurements of $\langle t_{\mathrm{esc}} \rangle$ versus slit height for devices with well controlled height variation ($\delta h_{\mathrm{max}} = 0.8\,\mathrm{nm}$, device class 1) and less well controlled height variation ($\delta h_{\mathrm{max}} = 10\,\mathrm{nm}$, device class 2); measurements taken for both device classes agree well. The relationship in Fig. 3(d) can be used to calibrate our tunable confinement system: calibration entails linking a given measurement of $\langle t_{\mathrm{esc}} \rangle$ to a corresponding charge value.

Calibration has two parts: firstly the DPW is linked to charge via[41,42]

$$W = \delta\psi_m q_{\mathrm{eff}}. \tag{1}$$

The quantity $\delta\psi_m$ is the difference in electric potential, averaged over the particle's surface, between the inside and outside of the well evaluated at the mid-point between the parallel device surfaces; $\delta\psi_m$ can be obtained from the Poisson-Boltzmann equation for known cavity geometry, effective and particle size (see Sup. Mat. V). The quantity q_{eff} is the particle's effective charge, the charge of the particle observed in a far field regime several Debye lengths away from the particle.[42] Secondly, Brownian Dynamics (BD) simulations are used to link $\langle t_{\mathrm{esc}} \rangle$ to the DPW. For this calibration, the plasmid's effective charge σ is obtained independently from electrophoresis ($q_{\mathrm{eff}} = -152 \pm 4e$). The plasmid's hydrodynamic radius r_H is fixed using the value from Newman *et al* (65 nm).[44] The missing parameter, the zeta potential of the confining surfaces ψ_s, is determined by finding the ψ_s value that brings the $\langle t_{\mathrm{esc}} \rangle$ values obtained from BD simulation into agreement with experiment (see Sup. Mat. VI). Figure 3(d) shows the final calibration curve obtained from Langevin simulations against $2h$ and ψ for q_{eff}, r_H. The dependence of $\langle t_{\mathrm{esc}} \rangle$ on $\delta\psi_m$ follows an exponential (Fig. 3(d), inset), in accordance with the Kramer relation:

$$\langle t_{\mathrm{esc}} \rangle = t_r \exp\left(\frac{q_{\mathrm{eff}}\delta\psi_m}{k_B T}\right) \tag{2}$$

with t_r a pre-exponential factor with dimension of time corresponding to a positional relaxation time (see Sup. Mat. IV).

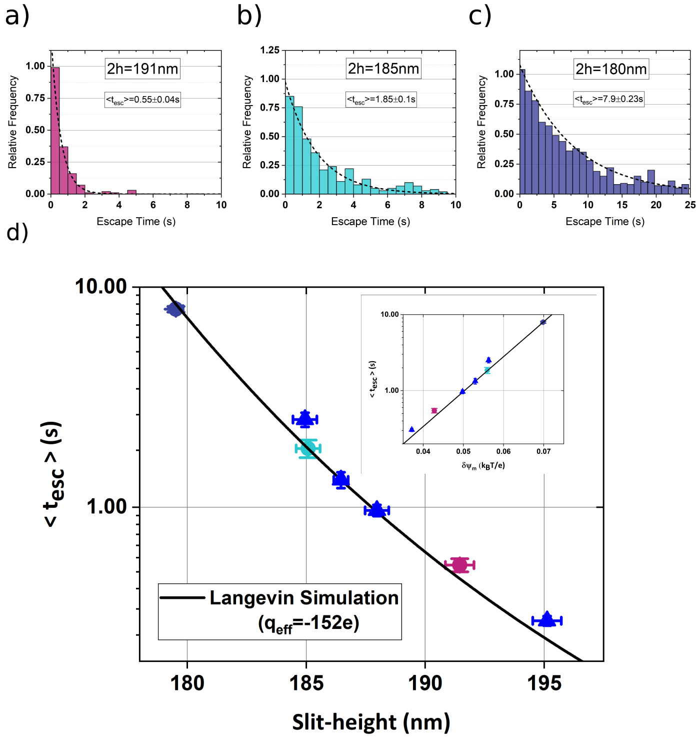

Figure 3: Normalized histogram of measured plasmid escape times for (a) slit height of 191 nm with 25 particles and 195 hopping events; (b) slit height of 185 nm with 42 particles and 351 hopping events; and (c) slit height of 180 nm with 74 particles and 295 hopping events. (e) Comparison of experimentally measured averaged escape times for different slit heights with Langevin simulation results. The inset gives the measured average escape time for different DPW on a log-linear scale with an exponential fit to the simulation results. Data points from device class 1 ($\delta h_{\max} = 0.8\,\text{nm}$) are shown as circles with colors that match the corresponding histograms in (a), (b) and (c). Data points from device class 2 ($\delta h_{\max} = 10\,\text{nm}$) are shown as blue triangles.

Next we use our calibrated system to perform simultaneous size and charge measurements on single confined vesicles (Fig. 4). Our EVs are obtained from the human glioblastoma astrocytoma (U373) and normal human astrocytoma (NHA) cell-lines, fluorescently labeled (with Dil) and suspended in 1mM Tris with 0.4 mM NaCl solution (see supporting information for details on EV isolation and preparation). Prior to introducing the EVs into our device, the EV size and charge were characterized respectively via Nanoparticle Tracking Analysis (NTA) and electrophorephoretic mobility. In addition, as a control, we investigated vesicles with a relatively more controlled, uniform chemistry: liposomes based on the phospholipid combination DOPC/Chol with incorporated Rhodamine DHPE dye (FormuMax Scientific Inc, US). Vesicle samples were introduced into our system and sufficient confinement was applied to fully isolate vesicles within individual cavities, completely preventing their escape. Then the confinement was reduced in $\approx 5\,\mathrm{nm}$ increments, with a $10\,\mathrm{s}$ hold after each confinement increment to observe if particle escape occurred. When particle escape was observed, the critical height was recorded and particle dynamics were integrated for $60\,\mathrm{s}$. Note that the critical height depends on the size and charge of particles. For the liposome sample, almost all particles escaped from the cavities at $2h = 291\,\mathrm{nm}$; however, for the EV sample, the critical confinement varied between 120 and 320 nm, hinting at the greater heterogeneity present in the EV sample. The t_{esc} can be obtained from analysis of single particle trajectories (Fig. 4(a)), with the measured $\langle t_{\mathrm{esc}} \rangle$ the average of the escape times for each trapping event. We have never observed occupancy of a single cavity by more than one vesicle, likely due to a self-exclusion effect arising from the vesicle's charge, i.e. the free energy of cavity occupancy of a charged vesicle is increased in the presence of a second like-charge vesicle due to strong repulsive electrostatic interactions between the vesicles. In order to obtain the vesicle hydrodynamic radius r_H, the vesicle mean square displacement (MSD, $\langle r^2 \rangle$) is obtained for the portion of the particle trajectory that is outside of the cavity, e.g. takes place completely in the surrounding slit (Fig. 4(b), $\langle r^2_{\mathrm{slit}} \rangle$). The diffusion constant and particle size is then inferred via $\langle r^2_{\mathrm{slit}} \rangle = 4Dt$ and the Einstein relation $D = k_B T/\zeta_{\mathrm{eff}}$. The quantity ζ_{eff} is a friction factor that takes hydrodynamic coupling between the particle and device surfaces into account using Faxén's approximation (see Sup. Mat. VII).

While measurements of $\langle t_{\mathrm{esc}} \rangle$ at a single confinement value can be used to deduce q_{eff}, this approach requires using Langevin simulations to deduce the exponential pre-factor t_r. Instead, using our ability to vary confinement experienced by a single vesicle, we reduce the confinement after the first measurement and perform a second integration over the dynamics to obtain $\langle t_{\mathrm{esc}} \rangle$ for an additional slit height $2h'$ (Fig. 4(c)). This second slit height was chosen

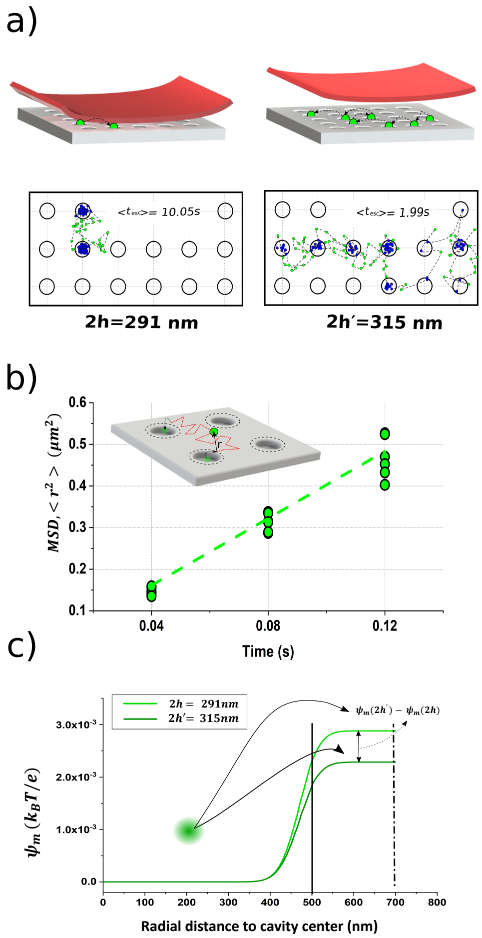

Figure 4: Methodology for measuring size and charge of single vesicles. (a) A sample trajectory of a liposome particle at two different slit heights ($2h = 291\,\mathrm{nm}$ and $2h' = 315\,\mathrm{nm}$) and resulting $\langle t_{\mathrm{esc}} \rangle$. (b) Mean square displacement in slit of 5 vesicles of similar size at the two different slit heights. The inset indicates the definition of the displacement vector $\mathbf{r}$ for a vesicle undergoing Brownian motion in the slit between cavities. (c) Mid-point potential measured for the two different slit heights.

by finding the minimum increment in $2h$ that yielded an appreciably lower $\langle t'_{\mathrm{esc}} \rangle$ (specifically, $\langle t'_{\mathrm{esc}} \rangle$ is 2-3 times smaller than $\langle t_{\mathrm{esc}} \rangle$ which is correlated to a 1-2 $k_{\mathrm{B}}T$ lower DPW).

For the liposome sample, $2h' = 315\,\mathrm{nm}$. For the EV samples, we observed that $2h'$ was typically 20-50 nm greater than $2h$ ($2h'$ =145-360 nm). By taking the ratio of the two average escape time measurements, from Eq. 2 we can deduce q_{eff} without knowledge of the exponential pre-factor:

$$q_{\mathrm{eff}} = \frac{1}{\psi_m(2h) - \psi_m(2h')} \log \frac{\langle t_{\mathrm{esc}} \rangle}{\langle t'_{\mathrm{esc}} \rangle}. \tag{3}$$

We used our device to characterize 30 liposome and 100 EVs for each of the EV samples (Fig. 5). Our results for both EV size (Fig. 5(a)) and zeta potential (Fig. 5(b)) are consistent with bulk approaches (i.e. electrophoresis and NTA), but our approach yields a correlated size and charge value for a single vesicle (Fig. 5(c)). To compare with electrophoresis measurements, our measured charge was converted to zeta-potential using a result derived from Poisson Boltzmann theory for spherical colloids[45,46] (see Sup. Mat. VIII). Note that, as expected, the EV samples have a considerably broader and more heterogeneous size and effective charge than the liposome sample. As the liposome sample are more chemically uniform than the EVs with a more tightly controlled diameter, the spread of the liposome measurements about the mean gives a measure of the expected error in a single vesicle measurement (technically, an upper limit in the single vesicle error as the liposomes are not completely mono-disperse). The measured mean±standard deviation for liposome diameter and zeta potential are respectively 239±8 nm and 38±2 mV, corresponding to one-sigma errors in vesicle diameter and zeta potential of respectively 3% and 5% (for comparison, the respective values from NTA and electrophoresis are 236±10 nm and 38.1±1.5 mV.) The liposome measurements were performed entirely with class 1 devices with well-controlled height ($\delta h_{\mathrm{max}} = 0.8\,\mathrm{nm}$). For the EV measurements, measurements were performed in both device classes, but predominantly in class 1. Measurements in both device type yielded equivalent means and distribution spreads (see Table S1 in Sup. Mat XI). The diameter dependence of the effective charge appears to roughly reflect a scaling $q_{\mathrm{eff}} \sim \zeta R^2$, with R the EV radius (see the inset to Fig. 5(c) which suggests that q_{eff} normalized to the EV surface area $4\pi R^2$, or equivalently zeta potential, is independent of diameter). The absence of particles below 60 nm in our sample is likely due to our use of a lipophilic stain; particles below 60 nm likely do not contain a lipid component.[10]

In addition, comparing the NHA and U373 secreted EVs shows that while the NHA and U373 EVs have a comparable size distribution (Fig. 5(a)), the NHA EVs are more highly charged (by about 18%, Fig. 5(b)). This difference is significant: the U373 EVs have a mean zeta potential of 41.3±0.6 mV, the NHA EVs have a mean zeta potential of 48.6±0.6 mV, with errors quoted corresponding to standard-deviation on the mean. Regarding the possible biological significance of this difference, it is well known that profound changes in membrane glycosylation occur in cancer. Although these changes usually lead to more sialylation and consequently more negatively charged EVs,[24] there are complicating effects, for example variability in negatively charged lipids like phosphatidyl serine[47] or changes in carbohydrate (HSPG) content of cellular membranes that spill over to EVs.[47,48] Also, the protein repertoire of EV surfaces is very different in cells that have undergone transformation, where hundreds of proteins appear or disappear as the cell acquire aggressive traits.[49] Lastly, different pathways of EV formation may be activated in cancer cells.[50]

In summary, we use tunable electrostatic confinement combined with single-molecule electrometry to characterize simultaneously the size and charge of EVs. Our configuration allows the confining potential to be varied over two orders of magnitude ($\sim$ 0.1 - 10 k_BT), allowing tuning of the particle escape rate from the wells. This tunable escape rate makes possible the extraction of the size/effective charge of single vesicles of differing size and charge measured in the array. While our current devices have a relatively small plateau region and hence throughput, increasing the total membrane area should be straightforward and then simple scaling suggests that we should be able to achieve throughputs $\sim$ 500 EV measurements per minute, with throughputs $\sim$ 1000 EV measurements per minute feasible with more concentrated samples that can ensure increased array occupancy (see

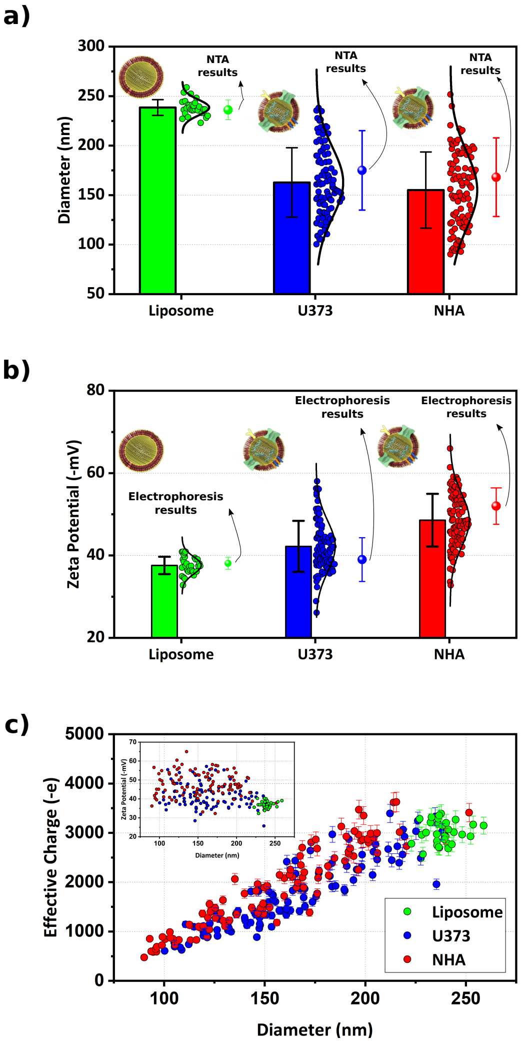

Figure 5: Size and charge measurement of 100 NHA (red) and 100 U373 (blue) EVs and 30 liposomes (green). (a) Distribution of diameter characterized in device. The small dots give results for individual vesicles measured in device, the bar gives the average over the individual vesicle measurements (with error-bar based on standard-deviation) and the large point to the right of the distributions gives the NTA result for comparison (with error-bar based on standard-deviation). (b) The zeta potential analysis for the same vesicles as in (a). The small dots give results for individual vesicles measured in device, the bar gives the average over the individual vesicle measurements (with error-bar based on standard-deviation) and the large point to the right of the distributions gives the electrophoresis result for comparison (with error-bar based on standard-deviation). (c) Scatter plot of effective charge versus diameter for the vesicles. Inset gives zeta potential versus diameter

Sup. Mat. XII). In addition, by fully deflecting the membrane lid, we can fully confine a vesicle in a single well. The tunable device, after extracting the charge and size of a single vesicle, might then potentially be able to isolate the vesicle in a single cavity where repeated chemical exchanges could lyse the EV, release the molecular cargo and then target the encapsulated RNA's and proteins for more detailed analysis. In particular, the ability to correlate the molecular repertoires of individual EVs with their size and charge, might give rise to new approaches for EV classification, complementary to isolation of EV subsets via flow-differentials.[10] Alternatively, we might stain EVs with fluorescent antibody conjugates specific to certain surface markers, and then use our approach to observe if these populations differ in their physical properties.

Acknowledgement

The authors thank Natural Science and Engineering Research Council of Canada (NSERC, G247765), New Frontiers for Research Fund-exploration (250326 NFRFE) and Canada Foundation for Innovation (CFI, G248924) for financial support. The authors acknowledge Nanotools-Microfab at McGill University and INRS Varennes. I.I.M. acknowledge Faculty of Engineering at McGill University for MEDA award.

Supporting Information Available

The Supporting Information is available free of charge via the internet at ACS Publications website.

The details on:

- Device fabrication
- Slit height calibration
- Measurement of solution ion concentration

- Calculation of particle escape time
- Solution for electrostatic potential
- Determining of zeta-potential of device surface
- Relationship between zeta potential and charge
- Automation of measurement
- Preparation of extracellular vesicles
- Data table for vesicle measurements
- Discussion of technology scaling

Also, Supporting Movie (MP4) is availble:

- Motion of a single YOYO-1 labeled pBR322 vector at different levels of confinements

References

(1) van Niel, G. Shedding light on the cell biology of extracellular vesicles. *Nature Reviews Molecular Cell Biology* **2018**, *19*, 213–228.

(2) van der Pol, E.; Böing, A. N.; Harrison, P.; Sturk, A.; Nieuwland, R. Classification, Functions, and Clinical Relevance of Extracellular Vesicles. *Pharmacological Reviews* **2012**, *64*, 676–705.

(3) Stahl, P. D.; Raposo, G. Extracellular Vesicles: Exosomes and Microvesicles, Integrators of Homeostasis. *Physiology* **2019**, *34*, 169–177.

(4) Nakano, I.; Garnoer, D.; Minata, M.; Rak, J. Extracellular vesicles in the biology of brain tumour stem cells – Implications for inter-cellular communication, therapy and biomarker development. *Seminars in Cell and Developmental Biology* **2015**, *40*, 17–26.

(5) Siravegna, G.; Marsoni, S.; Siena, S.; Bardelli, A. Integrating liquid biopsies into the management of cancer. *Seminars in Cell and Developmental Biology* **2017**, *14*, 531–548.

(6) Chao, H.; Im, H.; Castro, C. M.; Breakfield, R., Sandra; Weissleder; Lee, H. New Technologies for Analysis of Extracellular Vesicles. *Chemical Reviews* **2018**, *118*, 1917–1950.

(7) Raiborg, C.; Stenmark, H. The ESCRT machinery in endosomal sorting of ubiquitylated membrane proteins. *Nature* **2009**, *458*, 445–452.

(8) Trajkovic, K.; Hsu, C.; Chiantia, S.; Rajendran, L.; Wenzel, D.; Wieland, F.; Schwille, P.; Brügger, B.; Simons, M. Ceramide triggers budding of exosome vesicles into multivesicular endosomes. *Science* **2008**, *319*, 1244–1247.

(9) Zimmerman, B.; Kelly, B.; McMillan, B. J.; Seegar, T. C.; Dror, R. O.; Kruse, A. C.; Blacklow, S. C. Crystal structure of a full-length human tetraspanin reveals a cholesterol-binding pocket. *Cell* **2016**, *167*, 1041–1051.

(10) Zhang, H.; Freitas, D.; Kim, H. S.; Fabijanic, K.; Li, Z.; Chen, H.; Mark, M. T.; Molina, H.; Martin, A. B.; Bojmar, L., et al. Identification of distinct nanoparticles and subsets of extracellular vesicles by asymmetric flow field-flow fractionation. *Nature Cell Biology* **2018**, *20*, 332–343.

(11) Hugel, B.; Martínez, M. C.; Kunzelmann, C.; Freyssinet, J.-M. Membrane microparticles: two sides of the coin. *Physiology* **2005**, *20*, 22–27.

(12) Thomas, L. M.; Salter, R. D. Activation of macrophages by P2X7-induced microvesicles from myeloid cells is mediated by phospholipids and is partially dependent on TLR4. *The Journal of Immunology* **2010**, *185*, 3740–3749.

(13) D'Asti, E.; Chennakrishnaiah, S.; Lee, T. H.; Rak, J. Extracellular Vesicles in Brain Tumor Progression. *Cellular and Molecular Neurobiology* **2016**, *36*, 383–407.

(14) Inda, M.-d.-M.; Bonavia, R.; Seoane, J. Glioblastoma Multiforme: A Look Inside Its Heterogeneous Nature. *Cancers* **2014**, *6*, 226–239.

(15) Sawnton, C.; Pusztai, L.; Fisher, R. Cancer heterogeneity: implications for targeted therapeutics. *British Journal of Cancer* **2013**, *108*, 479–485.

(16) Jalali, M.; Hosseini, I. I.; AbdelFatah, T.; Montermini, L.; Hogiu, S. W.; Rak, J.; Mahshid, S. Plasmonic nanobowtiefluidic device for sensitive detection of glioma extracellular vesicles by Raman spectrometry. *Lab on a Chip* **2021**, *21*, 855–866.

(17) Sauter, E. R. Exosomes in blood and cancer. *Translational Cancer Research* **2017**, *6*, S1316–S1320.

(18) Liga, A.; Vliegenthart, D. B.; Oosthuyzen, W.; Dear, J. W.; Kerhoas-Kersaudy, M. Exosome isolation: a microfluidic road-map. *Lab-on-a-Chip* **2015**, *15*, 2388–2394.

(19) Zhao, Z.; Yang, Y.; Zeng, Y.; He, M. A microfluidic ExoSearch chip for multiplexed exosome detection towards blood-based ovarian cancer diagnosis. *Lab-on-a-Chip* **2016**, *16*, 489–496.

(20) Im, H.; Chao, H.; Park, Y. I.; Peterson, V. M.; Castro, C. M.; Weissleder, R.; Lee, H. Label-free detection and molecular profiling of exosomes with a nano-plasmonic sensor. *Nature Biotechnology* **2014**, *32*, 490–495.

(21) Williams, C.; Pazos, R.; Royo, F.; González, E.; Roura-Ferrer, M.; Martinez, A.; Gamiz, J.; Reichardt, N.-C.; Falcón-Pérez, J. M. Assessing the role of surface glycans of extracellular vesicles on cellular uptake. *Scientific Reports* **2019**, *9*, 1–14.

(22) Pfrieger, F. W.; Vitale, N. Cholesterol and the journey of extracellular vesicles. *Journal of Lipid Research* **2018**, *59*, 2255–2261.

(23) Mulcahy, L. A.; Pink, R. C.; Carter, D. R. F. Routes and mechanisms of extracellular vesicle uptake. *Journal of Extracellular Vesicles* **2014**, *3*, 24641.

(24) Akagi, T.; Ichiki, T. Evaluation of Zeta-Potential of Individual Exosomes Secreted from Biological Cells Using a Microcapillary Electrophoresis Chip. *Encyclopedia of Biocolloid and Biointerface Science 2V Set* **2016**, 469–473.

(25) Capaldi, X.; Liu, Z.; Zhang, Y.; Zeng, L.; Reyes-Lamothe, R.; Reisner, W. Probing the organization and dynamics of two DNA chains trapped in a nanofluidic cavity. *Soft Matter* **2018**, *14*, 8455–8465.

(26) Berard, D. J.; Leslie, S. R. Miniaturized flow cell with pneumatically-actuated vertical nanoconfinement for single-molecule imaging and manipulation. *Biomicrofluidics* **2018**, *12*, 054107.

(27) Berard, D. J.; Michaud, F.; Mahshid, S.; Ahamed, M. J.; McFaul, C. M.; Leith, J. S.; Bérubé, P.; Sladek, R.; Reisner, W.; Leslie, S. R. Convex lens-induced nanoscale templating. *Proceedings of the National Academy of Sciences* **2014**, *111*, 13295–13300.

(28) Shayegan, M.; Tahvildari, R.; Metera, K.; Kisley, L.; Michnick, S. W.; Leslie, S. R. Probing inhomogeneous diffusion in the microenvironments of phase-separated polymers under confinement. *Journal of the American Chemical Society* **2019**, *141*, 7751–7757.

(29) Thiombane, N. K.; Coutin, N.; Berard, D.; Tahvildari, R.; Leslie, S.; Nislow, C. Single-cell analysis for drug development using convex lens-induced confinement imaging. *BioTechniques* **2019**, *67*, 210–217.

(30) Shon, M. J.; Cohen, A. E. Mass Action at the Single-Molecule Level. *Journal of the American Chemical Society* **2012**, *134*, 14618–14623.

(31) Berard, D. J.; Miçhaud, F.; Mahshid, S.; Ahamed, M. J.; McFaul, C. M. J.; Leith, J. S.; Bérubé, R., Pierre; Sladek; Reisner, W.; Leslie, S. R. Convex lens-induced nanoscale templating. *Proced. Nat. Acad. Sci* **2014**, *111*, 13295–13300.

(32) Gerspach, M. A.; Mojarad, N.; Sharma, D.; Ekinci, Y.; Pfohl, T. Pneumatically Controlled Nanofluidic Devices for Contact-Free Trapping and Manipulation of Nanoparticles. *Part. Part. Syst. Charact.* **2018**, *35*, 1800161.

(33) Gerspach, M. A.; Mojarad, N.; Sharma, D.; Ekinci, Y.; Pfohl, T. Pneumatically Controlled Nanofluidic Devices for Contact-Free Trapping and Manipulation of Nanoparticles. *Part. Part. Syst. Charact.* **2018**, *35*, 1800161.

(34) Shayegan, M.; Tahvildari, R.; Metera, K.; Kisley, L.; Michnick, S. W.; Sabrina, L. R. Probing Inhomogeneous Diffusion in the Microenvironments of Phase-Separated Polymers under Confinement. *J. Am. Chem. Soc.* **2019**, *141*, 7751–7757.

(35) Ahamed, M. J.; Mahshid, S.; Berard, D. J.; Michaud, F.; Sladek, R.; Reisner, W. W.; Leslie, S. R. Continuous confinement fluidics: Getting lots of molecules into small spaces with high fidelity. *Macromolecules* **2016**, *49*, 2853–2859.

(36) Mahshid, S.; Lu, J.; Abidi, A. A.; Sladek, R.; Reisner, W. W.; Ahamed, M. J. Transverse dielectrophoretic-based DNA nanoscale confinement. *Scientific Reports* **2018**, *8*, 1–12.

(37) Mahshid, S.; Ahamed, M. J.; Berard, D.; Amin, S.; Sladek, R.; Leslie, S. R.; Reisner, W. Development of a platform for single cell genomics using convex lens-induced confinement. *Lab-on-a-Chip* **2015**, *15*, 3013–3020.

(38) Mojarad, N.; Krishnan, M. Measuring the size and charge of single nanoscale objects in solution using an electrostatic fluidic trap. *Nature Nanotechnology* **2012**, *7*, 448–452.

(39) Francesca, R.; Franziska, Z.; Natalie, M.; Magdelena, R. M. W.; Andrzej, O.; Benjamin, S.; Madhavi, K. Single-molecule electrometry. *Nature Nanotechnology* **2017**, *12*, 488–495.

(40) Ruggeri, F.; Krishnan, M. Spectrally resolved single-molecule electrometry. *J. Chem. Phys.* **2018**, *148*, 123307.

(41) Ruggeri, F.; Krishnan, M. Entropic trapping of a singly charged molecule in solution. *Nano Letters* **2018**, *18*, 3773–3779.

(42) Krishnan, M. A simple model for electrical charge in globular macromolecules and linear polyelectrolytes in solution. *J. Chem. Phys.* **2017**, *146*, 205101.

(43) Krishnan, M. Electrostatic free energy for a confined nanoscale object in a fluid. *J. Chem. Phys.* **2013**, *138*, 114906.

(44) Newman, J. Dynamic light scattering as a probe of superhelical DNA–intercalating agent interaction. *Biopolymers: Original Research on Biomolecules* **1984**, *23*, 1113–1119.

(45) Loeb, L., A; Overbeek, J. T. G.; Wiersema, P. H. *The electrical double layer around a spherical colloidal particle*; MIT Press: Cambridge, 1961.

(46) Krishnan, M.; Mojarad, N.; Kukura, P.; Sandoghdar, V. Geometry-induced electrostatic trapping of nanometric objects in a fluid. *Nature* **2010**, *467*, 692–695.

(47) Buzas, E. I.; Toth, E. A.; Sodar, B. W.; Szabo-Taylor, K. E. Molecular interactions at the surface of extracellular vesicles. *Seminars in Immunopathology* **2018**, *40*, 453–464.

(48) Martins, A. M.; Ramos, C. C.; Freitas, D.; Reis, C. A. Glycosylation of Cancer Extracellular Vesicles: Capture Strategies, Functional Roles and Potential Clinical Applications. *Cells* **2021**, *10*, 109.

(49) Choi, D.; Montermini, L.; Kim, D.-E.; Meehan, B.; Roth, F. P.; Rak, J. The Impact of Oncogenic EGFRvIII on the Proteome of Extracellular Vesicles Released from Glioblastoma Cells. *Molecular Cellular Proteomics* **2018**, *17*, 1948–1964.

(50) Spinelli, C.; Montermini, L.; Meehan, B.; Brisson, A. R.; Tan, S.; Choi, D.; Nakano, I.; Rak, J. Molecular subtypes and differentiation programmes of glioma stem cells as

determinants of extracellular vesicle profiles and endothelial cell-stimulating activities. *J. of Extracellular Vesicles* **2018**, *7*, 1490144.

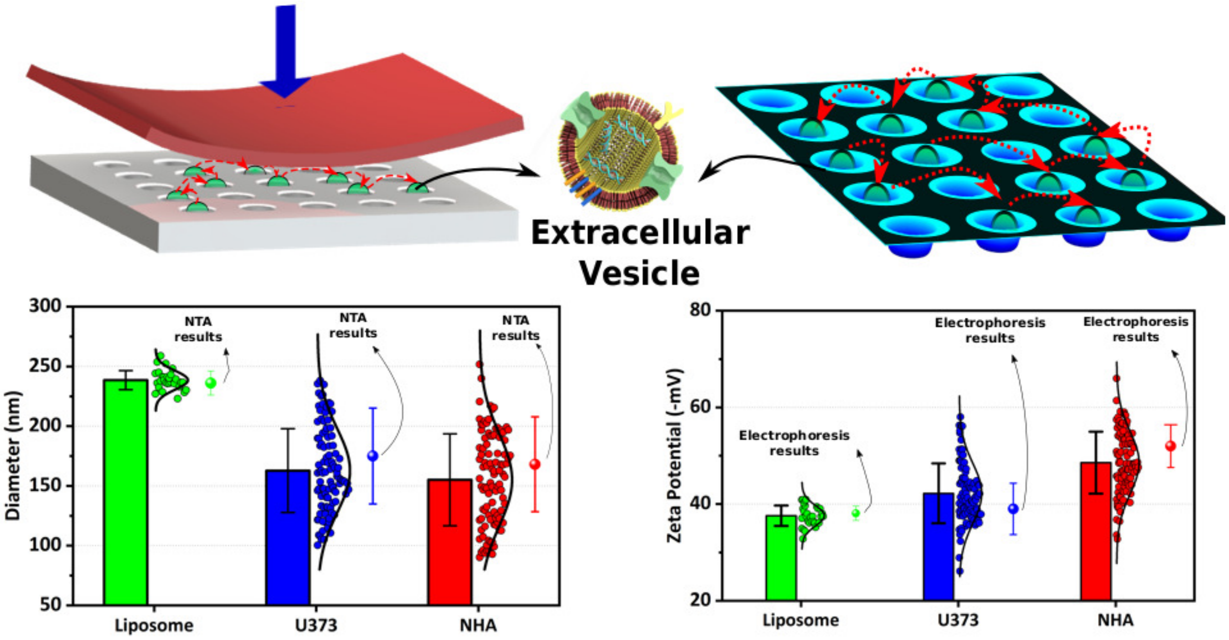

For Table of Contents Only